Title

First-Principles Characterization of Surface Phonons of Halide Perovskite CsPbI3 and Their Role in Stabilization

Journal

The Journal of Physical Chemistry Letters, 12(38)

ISSN

1948-7185

Authors

Yang, Ruo Xi

Tan, Liang Z

Publication Date

2021-09-30

DOI

10.1021/acs.jpclett.1c02515

Peer reviewed

First-principles characterization of surface phonons of halide perovskite $CsPbI_3$ and their role in stabilization

Ruo Xi Yang*,† and Liang Z. Tan*,‡

†*Materials Science Division, Lawrence Berkeley National Laboratory*

‡*The Molecular Foundry, Lawrence Berkeley National Laboratory*

E-mail: ruoxiyang@lbl.gov; lztan@lbl.gov

Abstract

The stability of halide perovskites has been a long standing issue for their real-world application. Approaches to improve stability include nanostructuring, dimensionality reduction and strain engineering, where surfaces play an important role in the formation of a stable structure. To understand the mechanism we compute the lattice dynamics of the surface of $CsPbI_3$ using density functional theory. We demonstrate, for the first time, that $CsPbI_3$ crystals exhibit surface phonons that are localized on the outermost layers of the slabs, and perform a complete symmetry characterization including an identification of the Raman/IR active modes. These surface phonons are present in the optically active cubic phase but are absent in the optically inactive "yellow" phase. Furthermore, we show that the surface suppresses bulk instabilities by hardening soft modes of the bulk cubic phase, resulting in phase stabilization and quenching of dynamical disorder. This study is fundamental for understanding the structural behaviour of halide perovskite materials with high surface area-to-volume ratios, and for guiding stabilization strategies.

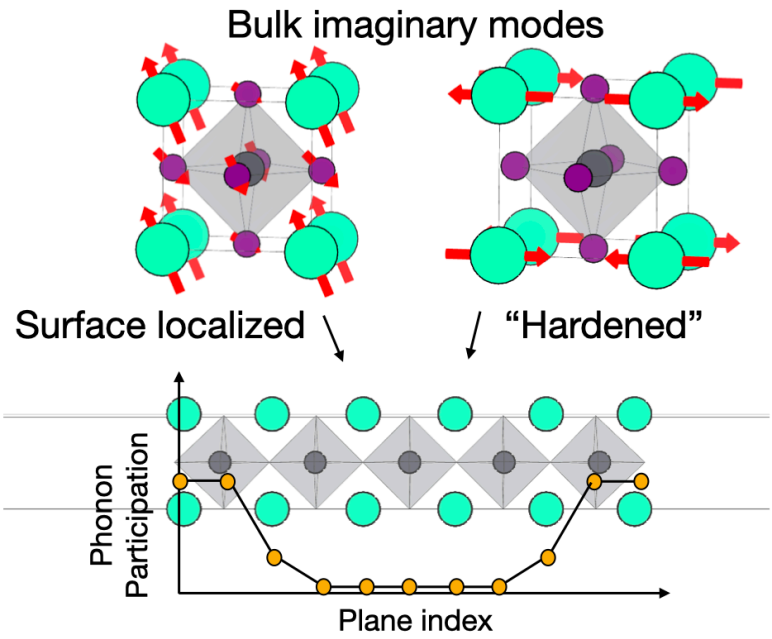
Bulk imaginary modes
Surface localized
“Hardened”
Phonon Participation
Plane index

Introduction

Lead halide perovskites have been considered the most promising photovoltaic material owning to their favorable electronic and optical properties, including high quantum efficiency, tunable band gaps, defect tolerance and high carrier mobility[1–3] While halide perovskites achieve high power generation efficiency in the laboratory, their long-term performance is compromised by the structural instability and chemical volatility, which causes the prototypical cubic crystal to break down under illumination, humidity and oxygen.[4–9] While the hybrid organic-inorganic halide perovskites $CN_3HN_3PbI_3$ suffer from chemical volatility, inorganic perovskites such as $CsPbX_3$ and $CsSnX_3$ (X = halide) present a different set of structural stability challenges.[10–12] Upon prolonged storage, the optically active α-phase cubic $CsPbI_3$ transforms into the undesired yellow phase (δ-phase) at room temperature, due to the low formation energy of the δ-phase at room temperature and the high flexibility of the perovskite lattice.[13,14] The types and magnitude of structural instabilities they adopt depend on the chemical compositions.

Surfaces and interfaces have been exploited as a strategy to stabilize the structure and tune transport properties of halide perovskites.[11,12,15–18] The truncation of the bulk materials alters the chemical environment and creates room for manipulation. For example, significant improvement in stability is observed in low dimensional perovskites, e.g. 2D perovskites Ruddlesden–Popper phase, where sheets of inorganic octahedra are sandwiched between organic cation and held by Coulomb forces, rendering them promising candidates for environmentally stable devices.[19–21] Another solution is the fabrication of quantum dots, of which enhanced phase stability compared to the bulk materials is observed. Decreased phase transition temperature to the cubic phase have been reported for these nanocrystals (NCs), suggesting the cubic phase are more readily stabilized in the NC forms.[11,12,22,23]

Numerous studies were done to understand the phase transition, in particular, the phonon behaviours of halide perovskites.[24–27] Raman/IR spectroscopy and X-ray diffraction (XRD) pair dis-

tribution function (PDF) are used to understand the structural dynamics in experiments, while phonon dispersion of bulk materials are routinely calculated using first-principles methods.[26,28,29] However, a thorough study on the structural behaviour of the low dimensional halide perovskites have been lacking. Similar to the bulk where soft modes lead to double well potential in structural dynamics,[24,25] soft modes of the surface are likely to dominate the energy landscape in nanostructures, providing strategies for better stabilization. In addition, luminescence from bulk perovskites are known to be affected by phonons,[30] and surface phonons are likely to behave similarly and affect the optical properties of perovskites quantum dots/slabs.[31,32]

Other than perovskites, surface phonons have been reported in traditional NC materials such as Si, ZnO and CdS.[33–35] Raman peak shift and broadening as a function of the NC size are observed in these materials, which is attributed to finite size effect as well as surface phonons. For halide perovskites, the picture is complicated by a more complex structure and dynamical structural instabilities.

In this work, we used density functional theory (DFT) to calculate the phonon properties of $CsPbI_3$ slabs of two phases: optically active cubic phase (α phase), and the optically inactive yellow phase (δ phase). We identified a number of surface localized phonon modes via attenuation curves. We performed a complete characterization of these surface modes, including their Raman and IR activity. These surface phonon modes have a penetration depth of 1-2 atomic layers into the surface, and consist of both in-plane and out-of-plane displacements. We found that one imaginary mode at the Γ-point in the bulk becomes surface localized, which facilitates its control via surface engineering. Another imaginary mode at the M-point, i.e. the Cs head-to-head mode in the bulk, is "hardened" in the surfaces, meaning the structure becomes stable against that particular fluctuation. Finite nanocrystal size effects modify some of the Raman/IR selection rules of the surface modes, which we tabulate according to their irreducible representations (irrep). These results show that, the roles of surfaces must be considered in the stability of 2D and nanocrystal halide perovskites.

Methods

The crystal structure of cubic phase and orthorhombic yellow phase $CsPbI_3$ are fully relaxed using Density functional theory (DFT) as implemented in the pseudopotential plane-wave code VASP[36,37] with PBEsol functional.[38–40] A plane-wave kinetic-energy cutoff of 800 eV and an electronic Brillouin zone sampling with an $8 \times 8 \times 8$ k-point mesh for the cubic and $6 \times 6 \times 8$ for the yellow phases are used. The convergence criteria for total energy and forces is 1×10^{-6} eV, and 1×10^{-3} eV/Å. The bulk crystal structure is used to construct the slabs for each phase. Here we used the (100) facet with CsI termination as it has been shown to be the most stable surface with the lowest surface energy.[41] The lattice parameters are adopted from the bulk values, which are 6.25 Å for the cubic, and a = 10.42 Å, b = 4.76 Å for the yellow phase. The unit cell of the slab are kept fixed but the internal atomic positions are fully relaxed. The crystal structures of the slab models are shown in the Supporting Information (SI Fig.1). For the yellow phase the slab model is stoichiometric with crystal formula of $Cs_6Pb_6I_{18}$, and for the cubic phase it is non-stoichiometric with the formula $Cs_6Pb_5I_{16}$. Convergence of surface energy has been tested against the number of layers, resulting in the adoption of 5-octahedra-layer slabs for the cubic phase and 3-octahedra-layer for the yellow phase. The vacuum size is chosen to be larger than 30 Å to minimize the influence from the opposite surface. The surface is parallel to the $x-y$ plane, normal to the z direction.

Phonon calculations are carried out using the finite displacement method using both VASP and Phonopy.[42] $2\times2\times2$ supercells are constructed with an array of symmetrised atomic displacement to obtain the force constants, using a displacement amplitude of 0.01 Å. The surface Brillouin zone (BZ) contains the high symmetry points: $\bar{\Gamma}$ (0, 0, 0), $\bar{M}$ (0.5, 0.5, 0) and $\bar{X}$ (0, 0.5, 0), shown in Fig.1. In this study, we mark the high-symmetry points in surface BZ with a bar, and bulk BZ without it.

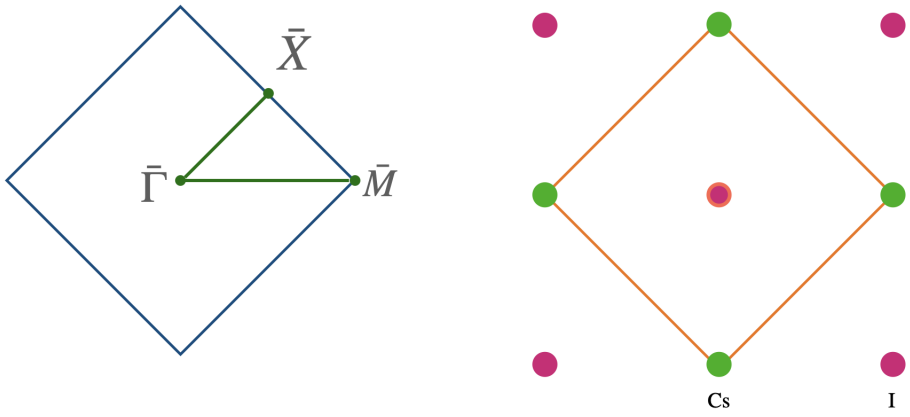

Figure 1: Left: The surface Brillouin zone with the labeled Q-point. Right: the primitive cell in real space.

Results and discussion

Phonon dispersion

Comparing the phonon dispersion of the slab and bulk structures for each phase (Fig.2), we find several differences. The surface phonon band structure contains more bands than the bulk band structure due to larger number of atoms in the simulation cell. For many of these bands, their frequency and dispersion are largely similar between the slabs and the bulk — these correspond to bulk phonon modes. Besides these, we find new surface phonon modes that are present only in the surface simulation, as well as modes that have different frequencies in the bulk and at the surface, mostly occurring in the low and imaginary frequency region.

We note that the surface phonon band structure contains bulk phonon bands that can have a different q-vector in the bulk than shown in the surface band structure plot (Fig.2). In general, a phonon band at $q = (q_x, q_y, 0)$ in the slab calculation can be unfolded to a bulk phonon at $q = (q_x, q_y, q_z)$ in the bulk calculation.[43] For example, the X-point in the bulk contains only a single imaginary phonon frequency, while the $\bar{X}$-point in the surface contains many. These are in fact $\bar{X}$-point (0,1/2,0) modes which are unfolded to bulk imaginary modes at the M-point (1/2,1/2,0),

and should not be mistaken for new surface modes. Similarly, some of the flat bands in the surface band structure plot at $q = (q_x, q_y, 0)$ (marked by black dots in Fig. 4) are unfolded to bulk phonon bands at $q = (q_x, q_y, 2\pi n/L)$, where n ranges over the number of unit cells in the slab of thickness L. These flat bands are not entirely dispersionless, they are flat in the $q_x - q_y$ plane, but have a dispersion in q_z, which explains why they occur at different frequencies in the bulk and surface band structure plot. These types of modes, due to their bulk-like nature, will not be discussed in detail in this paper.

For the cubic phase, there are numerous phonon modes that are true surface modes, in that they are localized at the surface and are not just projections of bulk phonon modes. Besides these features, both the bulk and the slab cubic phases showed imaginary frequencies across the BZ, particularly at M ($\bar{M}$) and X ($\bar{X}$) point, which is mostly attributed to octahedral tilting. At Γ ($\bar{\Gamma}$) point, the imaginary branch for the bulk is -0.54 THz (opposite displacement of Cs and I), and for the slab -0.41 THz (similar character as the bulk). For higher-lying optical branches, the frequencies are almost identical (< 0.01 THz difference). The cubic phase has an additional distinct feature at the $\bar{M}$-point: the lowest positive frequency branch at 0.1 THz is separated from the rest of the phonon bands, has an undulating shape, and is absent in the bulk band structure (green box in Fig. 4). We refer to this mode as a "hardened" $\bar{M}$ mode, which will be further discussed below.

We calculate the phonon projected density of states (PDOS) on to the surface planes and the interior planes (Fig.4b) from cubic phase. It is clear that the most of the imaginary modes still belong to the bulk, although part of it are confined on the surface. Many of the surface phonons are resonant with the bulk phonons with frequencies buried in the bulk spectrum. However, there are two peaks in the surface phonon DOS at 1.2 THz and 1.5 THz , suggesting localized states with density higher than the bulk signals. The 1.2 THz Raman peak belongs to $\bar{\Gamma}$-point group 3 mode with irrep Γ_5, and the 1.5 THz Raman peak belongs to the $\bar{M}$-point group 1 mode with irrep M_1. (Table 1 and Fig.4a)

In comparison, the yellow phase does not exhibit noticeable features for the slabs. Both the bulk and slab do not show imaginary frequencies, indicating a stable structure. The frequency

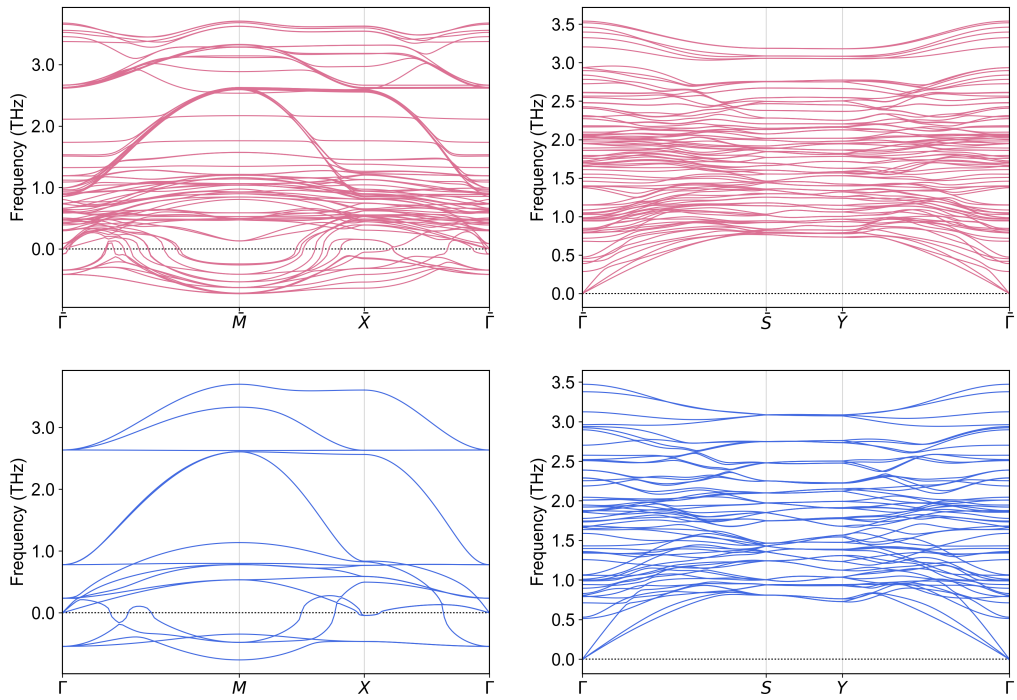

Figure 2: Phonon dispersion of cubic (left column) and yellow phase (right column), respectively. Top panel for the slabs and bottom panel for bulk.

differences between bulk and slab calculations for each branch is also negligible.

While the characteristics of the phonon dispersion of both bulk and slabs are very similar, it is not sufficient to rule out the possibilities of localised states as they may be "hidden" in the bulk branches. In the following section we introduce an approach to identify such surface modes, and to distinguish them from modes unfolded to other q-points in the bulk band structure.

Identification of surface phonon modes

To differentiate surface phonon modes from bulk-like modes in the calculation, we examine the attenuation of the phonon wavefunctions as a function of distance from the surface. For a given phonon mode of eigenvector e, the weight of one atom contributing to the mode is given by:

$$w_n(i) = \sum_{\beta}^{3} |e_i|^2[\beta] \tag{1}$$

where i denotes the atom index, n the phonon mode, β the Cartesian direction. $w(i)$ should be compared to unity, since $\sum_N w(i)$ has a norm of one. Similarly, we define the participation of a plane in a certain phonon mode as:

$$P_{\text{plane}}(n,c) = \sum_{j \in c} w_n(j) \tag{2}$$

where c denotes the plane index, and j is the atom index that belongs to plane c. $P(n,c)$ quantifies the weight of a plane c that contributes to the eigenvectors of a phonon mode n.

We then plot the $P(n,c)$ for certain planes of the slab for a particular mode. Here we chose three high-symmetry points in the BZ: $\bar{\Gamma}$-point (0, 0, 0), $\bar{M}$-point (0.5,0.5,0.0) and $\bar{X}$-point (0.0, 0.5, 0.0) , and calculated the $P(n,c)$ for each band. The results of the cubic phase are shown in Fig.3. The surface modes are distinguished by attenuation curves that are strongly peaked at the surface, and decrease to zero in going from the outer-most layers of the slab into the bulk region. On the other hand, bulk modes contain appreciable phonon weight deep into the central layers of the slab. Some of the bulk modes have weights strongly peaked in the central layers of the slab (SI Fig.2). This is likely to be an artefact of the finite size simulation, and is expected to be distributed more homogeneously as the number of layers is increased. These attenuation curves therefore unambiguously identify the surface modes.

For the cubic phase, there are a number of surface localized modes at $\bar{\Gamma}$-point, $\bar{M}$-point and $\bar{X}$-point as shown in Fig.3. In comparison, for the yellow phase, there is no such pattern for the participation $P(n,c)$, indicating that there is no surface localized phonon modes. With the q-point and the band index, we can then mark these modes in the cubic phase phonon band structure in Fig.4a. The character of these modes will be discussed in the following section.

In electronic structure theory, the inverse participation ratio (IPR), defined as $\text{IPR}(y) = \sum_i^N y_i^4 / (\sum_i y_i^2)^2$, has often been employed to quantify the localization of states, where y_i is the eigenvector for state i, and N is the total number of states. IPR = 1/N represents completely delocalized states, and IPR = 1 for completely localized state. A delocalized phonon would have an IPR proportional to $1/n$ (n

$\rightarrow \infty$), when n is a large number of unit cells. However, in practice, phonon calculations can only be scaled up to a moderate number of atoms at the DFT level. We therefore use the attenuation curve to identify the surface localized states here.

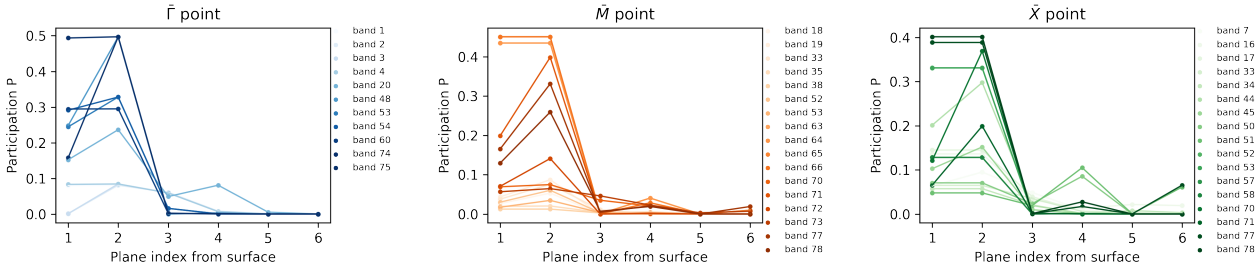

Figure 3: Attenuation curves of surface modes, showing the participation P for different planes in the cubic slab. The plane index denotes atomic planes starting from out-most layer and counting inwards into the center. Odd numbered planes are CsI, and even numbered planes are PbI_2. Only half of the planes are shown here as the slab is symmetrical. The legend shows the band index, counting from bottom of the dispersion. The three columns correspond to $\bar{\Gamma}$, $\bar{M}$ and $\bar{X}$ point, respectively.

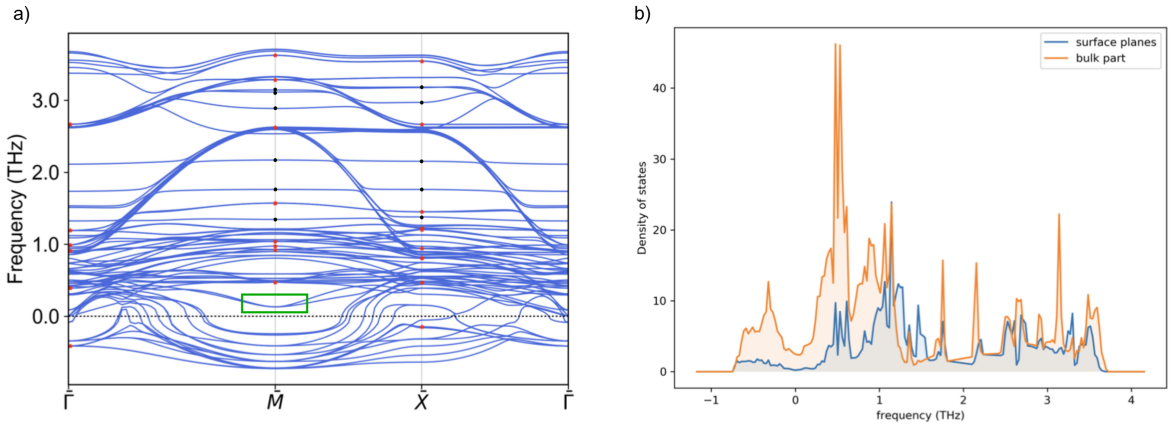

Figure 4: Surface phonon modes of the cubic phase. a) Phonon dispersion of the cubic slabs with red stars marking the surface modes. The green box marks the "hardened" mode from the bulk. The black dots mark the "flat band" that can be unfold to bulk-like phonons in the q_z direction. b) PDOS of the surface modes and the bulk modes.

Table 1: Table of all cubic phase surface modes categorized by their characterization. The first-order IR/Raman activity is tabulated for the $\bar{\Gamma}$ modes, and the second-order IR/Raman activity is tabulated for the zone-boundary modes ($\bar{M}$ and $\bar{X}$ points), which all exhibit second-order IR/Raman activity. Irreps are tabulated for the single-surface (P4mm) and for the symmetric slab (P4/mmm) cases. The pair of irreps under the P4/mmm column correspond to in-phase and out-of-phase combinations of the single-surface modes.

		Frequency (THz)	Characterization	irrep (P4mm)	irrep (P4/mmm)	IR/Raman activity
$\bar{\Gamma}$	Group1	-0.415	Imaginary	Γ_5	Γ_5^+, Γ_5^-	IR/Raman
	Group 2	0.39	Out-of-plane Cs and I displacement	Γ_1	Γ_1^+, Γ_3^-	IR/Raman
		0.91	Out-of-plane I displacement	Γ_2	Γ_2^+, Γ_4^-	Raman
		1.51	Out-of-plane Cs and I displacement	Γ_1	Γ_1^+, Γ_3^-	IR/Raman
	Group 3	0.99	In-plane Pb displacement	Γ_5	Γ_5^+, Γ_5^-	IR/Raman
		1.19	In-plane Cs and I displacement	Γ_5	Γ_5^+, Γ_5^-	IR/Raman
		2.67	In-plane JT distortion	Γ_5	Γ_5^+, Γ_5^-	IR/Raman
$\bar{M}$	Group 1	0.47	Octahedral tilting	M_1	M_1^+, M_3^-	2nd-order
		0.92	Octahedral tilting + out-of-plane Cs displacement	M_1	M_1^+, M_3^-	2nd-order
		1.57	Octahedral tilting + out-of-plane Cs displacement	M_1	M_1^+, M_3^-	2nd-order
	Group 2	0.97	Out-of-plane cation displacement	M_1	M_1^+, M_3^-	2nd-order
		1.04	In-plane cation displacement	M_5	M_5^+, M_5^-	2nd-order
		2.63	In-plane cation displacement	M_5	M_5^+, M_5^-	2nd-order
		2.63	In-plane cation displacement	M_5	M_5^+, M_5^-	2nd-order
	Group 3	3.28	Out-of-plane JT distortion	M_1	M_1^+, M_3^-	2nd-order
		3.29	In-plane JT distortion	M_3	M_4^+, M_2^-	2nd-order
	Group 4	3.62	In-plane octahedral breathing	M_4	M_3^+, M_1^-	2nd-order
$\bar{X}$	Group 1	-0.14	Imaginary	X_1	X_1^+, X_2^-	2nd-order
	Group 2	0.47	Octahedral tilting + in-plane Cs displacement	X_3	X_3^+, X_4^-	2nd-order
		0.80	Octahedral tilting + out-of-plane Cs displacement	X_1	X_1^+, X_2^-	2nd-order
		1.20	Octahedral tilting + out-of-plane Cs displacement	X_1	X_1^+, X_2^-	2nd-order
		1.22	Octahedral tilting + out-of-plane Cs displacement	X_3	X_3^+, X_4^-	2nd-order
		1.45	Octahedral tilting + out-of-plane Cs displacement	X_1	X_1^+, X_2^-	2nd-order
	Group 3	0.94	In-plane JT distortion	X_3	X_3^+, X_4^-	2nd-order
		2.67	In-plane JT distortion	X_3	X_3^+, X_4^-	2nd-order
	Group 4	3.54	In-plane breathing mode	X_4	X_4^+, X_3^-	2nd-order

Categorization of surface phonon modes

The symmetries of the surface phonon modes are characterized by direct examination of their eigenvectors. Due to the complex nature of these modes, we categorized them first based on the q-point of each mode: at $\bar{\Gamma}$, $\bar{M}$, $\bar{X}$, and then by their symmetries and character at each q-point. The space group of our simulation of a symmetric slab is P4/mmm, with the two surfaces the slab chosen to be inversion symmetric, for simplicity. However, the experimental situation may contain a breaking of the mirror symmetry between the two surfaces, such as one surface being exposed to a different substrate or environment than the other surface. In such a situation, the space group would be P4mm instead, with each surface being considered independently from the other. Therefore, we consider both symmetries when assigning irreps to the surface phonon modes (Table 1). The symmetric slab case (P4/mmm) contains twice the number of irreps as the single-surface case (P4mm), because the single-surface modes can be combined either in-phase or out-of-phase. Symmetry assignments were performed by comparing mode eigenvectors to character tables of the k-points under P4/mmm or P4mm.[44] In the following discussion, we use the irreps of the single-surface to refer to the modes.

$\bar{\Gamma}$ *modes*: After accounting for symmetry, surface phonon modes reduce to the following 3 groups. (Fig.5 and summarized in Table.1)

Group 1, the imaginary mode, has Cs and I moving with opposite displacements, which is similar to the Γ-point imaginary mode of cubic bulk $CsPbI_3$. This mode is 2-fold degenerate with displacements pointing to the x and y direction, and has an irrep of Γ_5.

Compared to the bulk imaginary modes at the Γ-point, these surface modes localize at the top layer of the surface. Secondly, the absolute value of the frequency is smaller (-0.42 THz) than the bulk (-0.54 THz). This indicates that this mode is slightly less unstable than in the bulk, as it has a less negative local curvature about the equilibrium structure.[25] Group 2 features the out-of-plane modes.

In the 0.39 THz Γ_1 mode, Cs, I, and Pb simultaneously move towards the center of the slabs. The 0.91 THz mode consists of first layer octahedra distortion via the opposite displacements of

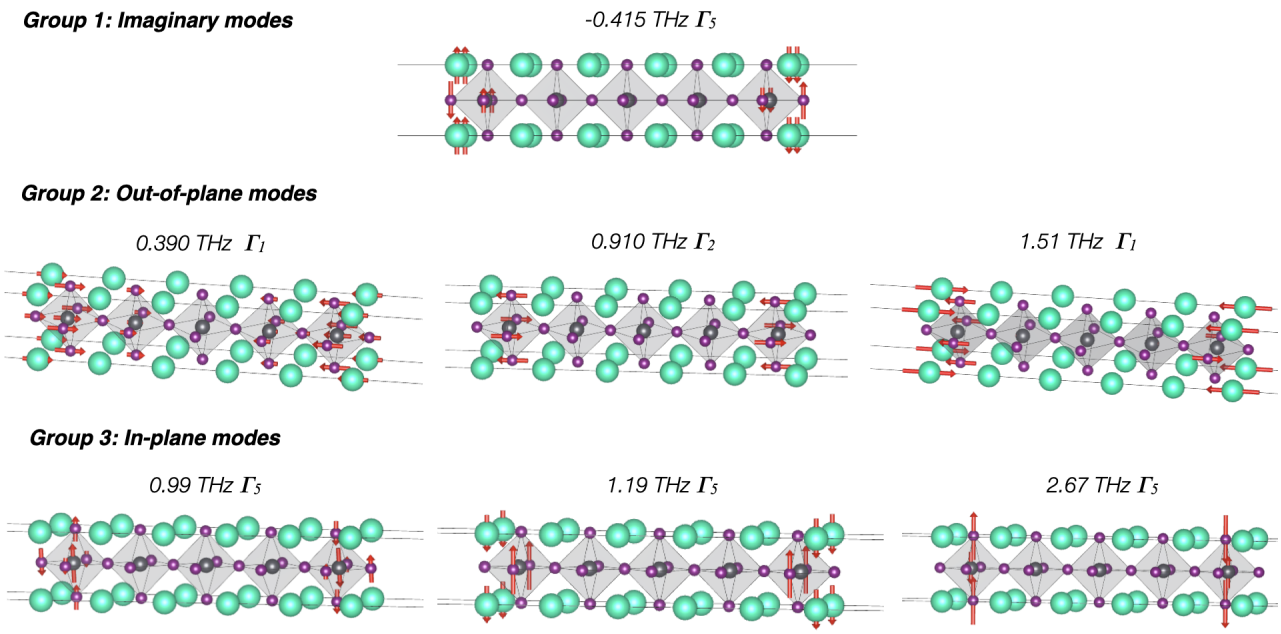

Figure 5: The $\bar{\Gamma}$-point surface modes schematics of cubic $CsPbI_3$. The red arrow represents the eigenvectors. The frequencies and the IRREPs are denoted.

neighbouring I atoms, with an irrep of Γ_2. In the 1.51 THz mode, the surface Cs and I move towards each other (irrep Γ_1). The 0.39 THz Γ_1 mode can be compared to an acoustic-like mode that involves the surface atoms only, while the 1.51 THz Γ_1 mode can be compared to an optical-like mode that involves surface atoms only. Accordingly, the 0.39 THz Γ_1 mode has a lower frequency.

Group 3 includes in-plane modes with frequency 0.99 THz, 1.19 THz, and 1.57 THz. Each of these modes has a 2-fold degeneracy corresponding to x and y direction displacements, and has an irrep of Γ_5. The 0.99 THz mode and 1.57 THz mode feature the the Jahn-Teller (JT) distortion of the octahedra at the surface, where the Pb-I bond either shortens or elongates, accompanied by the off-center motion of Pb. These two modes resembles two optical modes in the bulk, which also adopt Jahn-Teller type distortion with similar frequencies. Unlike group 1, these modes posses higher frequencies than the same modes in the bulk. The 1.19 THz mode has opposite displacements of surface Cs and I, which do not resemble any bulk modes.

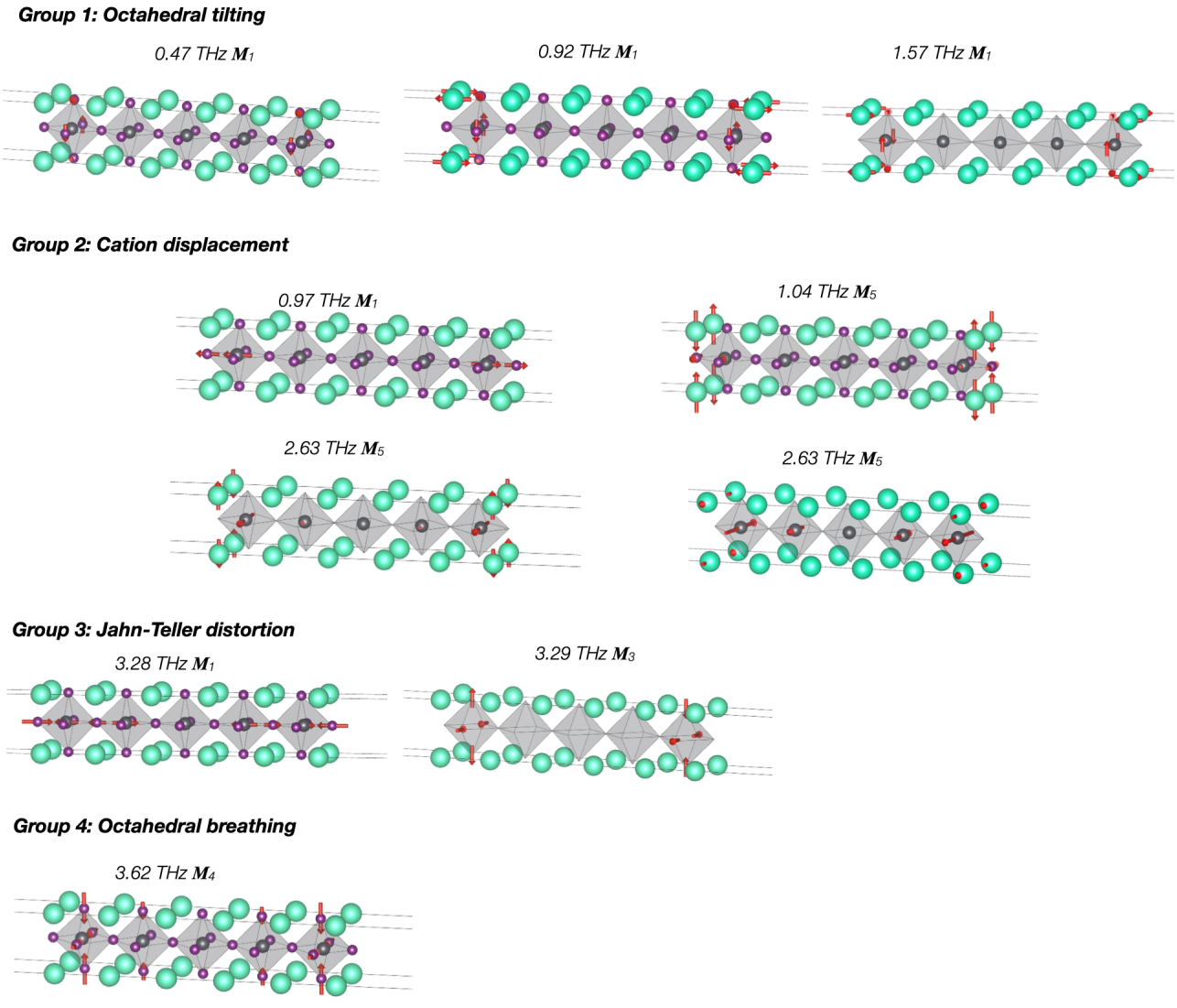

Figure 6: Surface modes at $\bar{M}$-point of cubic $CsPbI_3$ with the corresponding frequencies and irreps denoted. I atoms (purple circle) are omitted sometimes for clearer visualisation.

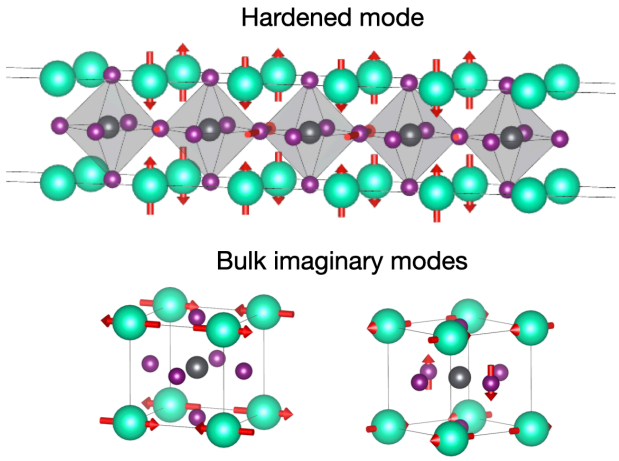

Figure 7: "Hardened" mode and its comparison with the bulk imaginary modes. Both are at M-point ($\bar{M}$).

$\bar{M}$ modes: the surface modes at $\bar{M}$-point are shown in Fig.6. Similar to the $\bar{\Gamma}$-point modes, there are several groups of modes that we categorize in the following paragraphs.

Group 1 modes at $\bar{M}$-point involve in-plane octahedral tilting that only happen at the top layer of octahedra, owing to its zone-boundary nature. These modes include 0.47 THz M_1 mode, 0.92 THz M_1 mode, and 1.57 THz M_1 mode, where the latter two are accompanied by the off-center displacements of Cs at the top layer too.

Group 2: these modes are mostly cation displacements of Cs or Pb atoms at the top 2 layers of the surface. 0.97 THz M_1 mode adopts the out-of-plane motion of Pb, and the 1.04 THz M_5 mode adopts the in-plane motion of Cs and Pb, both accompanied by the displacement of I at the top layer. The two 2.63 THz M_5 modes are both doubly degenerate in the x and y directions, both entailing the off-center displacement of Pb and Cs. The difference is that in the former Cs and Pb move perpendicular to each other and parallel in the latter.

Group 3: Going to higher frequency, the surface modes mainly involve the Jahn-Teller (JT) distortion, either in-plane or out-of-plane. The 3.29 THz M_3 mode belongs to in-plane JT distortion, and another 3.28 THz M_1 mode are out-of-plane.

Group 4: there is also a breathing mode with irrep M_4 at 3.62 THz where the octahedra within the plane unit cell contracts or expands, with 4 Pb-I bonds either shorten or elongate (different to

JT distortion). Similar to JT distortion, it occurs at rather high frequency.

Note that the order of the frequencies which these modes adopt is: octahedral tilting modes < cation displacements < Jahn-Teller distortion < breathing modes. The reason lies in the strength of the recoil force for each mode, where octahedral tilting and A-site cation displacement are dictated by changes in the electrostatic potential where interaction is weak due to singly charged cations, while Jahn-Teller distortion and the breathing mode are directly associated with stronger Pb-I bonding.

Interestingly, the lowest (positive) frequency 0.1 THz mode at the M-point appears to be remarkably similar to the bulk imaginary modes (Fig.7), both containing head-to-head displacements of Cs ions with simultaneous halide breathing displacements, which has been identified as a dominant contributor to dynamic disorder in bulk halide perovskites.[26] This 0.1 THz mode at the $\bar{M}$-point is a bulk-like mode that can be understood as being a hardened version of the bulk imaginary modes. The M_5 surface mode at 1.04 THz at the $\bar{M}$ point also contains head-to-head Cs displacements, and can likewise be interpreted as being lifted in frequency from the bulk imaginary head-to-head modes. Therefore, the effect of nanostructuring is to remove one primary mechanism of structural fluctuations of the surface. As a result, the cubic surface is stabilized relative to the cubic bulk, and the overall stability of a nanocrystal or a finite slab increases with its surface-to-volume ratio.

Not only is the surface stabilized by a large amount, but also the interior of the slab, although to a lesser extent. The mode hardening at the surface can be understood as arising from missing halide atoms due to cleavage of the surface plane. In the bulk, these halide ions mediate head-to-head motion of Cs ions by performing a concerted breathing motion.[26] In the absence of this mechanism at the surface, the mode is hardened, with its effect persisting into the interior of the slab for at least as far as the size of this simulation. This is an intrinsic effect of the surface itself, and is independent of ligand anchoring effects which may also affect nanostructure stability.

$\bar{X}$-point modes are rather similar to the behaviour of $\bar{M}$-point modes (Table 1). Like the $\bar{M}$-point, the $\bar{X}$-point contains octahedral tilting (with X_1 and X_3 irreps), Jahn-Teller distortions (X_3),

and in-plane breathing modes(X_4) (characterization in SI.Fig.S3). The difference between $\bar{X}$-point and $\bar{M}$-point is that for $\bar{X}$-point modes, the atoms in the neighbouring unit cell are moving out of phase in a single in-plane direction, while for $\bar{M}$-point modes in two directions (x and y). There is an imaginary surface mode (-0.14 THz) at $\bar{X}$-point (Fig.8), with X_1 symmetry, where two I atoms from the first layer of octahedra move parallel away from the high-symmetry point. This mode does not appear in the bulk imaginary modes at X-point.

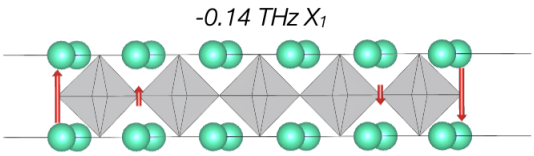

Figure 8: $\bar{X}$-point imaginary mode of cubic $CsPbI_3$ with the corresponding frequencies and irrep denoted.

We notice one important distinction between the $\bar{\Gamma}$-point and the $\bar{M}$ point surface modes: while the surface modes at the $\bar{M}$ point all have real frequencies, the $\bar{\Gamma}$-point has one imaginary frequency surface localized mode. With the $\bar{M}$-point head-to-head instability removed from the surface, the Γ_5 imaginary surface mode becomes the primary instability of the surface, with the X_1 imaginary surface mode being of a smaller magnitude imaginary frequency. The bare surface thus is primarily susceptible to polar in-plane fluctuations. This suggests that structural stabilization in nanostructure perovskites can potentially be achieved via suppression of at least the Γ_5 imaginary surface mode, and ideally the X_1 imaginary surface mode as well. First, the imaginary phonons are partially localized at the surface via nanostructuring, and then the surface phonons can be stabilized through ligands or interfaces, providing a convenient way to control the structural stability of these compounds. In experiments, ligand passivation and lattice anchoring in 2D or nanocrystal perovskites have been shown to be excellent stabilization methods.[45,46]

The organic-inorganic hybrid perovskites such as methylammonium halide perovskites or formamidinium perovskites have similar structures and suffer from similar structural instabilities. However, they also experience chemical volatility due to the organic molecules. Therefore, while

the surface phonon behaviours could potentially be similar in these two systems, they need to be individually investigated.

Raman/IR detection of surface phonon modes

Optical spectroscopies such as Raman and IR absorption are widely used for the characterization of vibrational properties, including $CsPbI_3$.[47–50] Here we consider the detection of surface phonon modes using these experimental techniques. Knowing that Γ_1 and Γ_5 are IR active, and that Γ_1, Γ_2, Γ_3, Γ_4 and Γ_5 are Raman active, we tabulate the one-phonon IR/Raman activity of $\bar{\Gamma}$-point surface modes in Table 1, with all $\bar{\Gamma}$-point surface modes being Raman active. Here we consider unpolarized light; further differentiation of the surface modes may be made by considering polarization directions and incidence geometries. Other spectroscopies such as spatially resolved electron energy loss spectroscopy (EELS) is also useful for resolving these vibrational properties.[34,51,52]

Momentum conservation often restricts these optical spectroscopies to detection of phonons of wavevector q close to the Γ point, as $\hbar k_s = \hbar k_l \pm \hbar q$ where $k_s(k_l)$, the wavevector of the scattered(incident) light, is much smaller than the Brillouin zone $2\pi/a$, a being the lattice constant. Nevertheless, non-$\bar{\Gamma}$ point phonons involved in two-phonon processes may still be detectable. To analyze the IR/Raman activity of the $q \neq 0$ phonons, we check if the product representations of the modes, D^2, contains the irrep of a vector (for the case of IR), or the irrep of a symmetric second rank tensor (for Raman),[53] where the mode irreps D are taken from Table 1. For the single-surface modes (P4mm), We find that all overtones of the $\bar{M}$ and $\bar{X}$ modes are IR and Raman active. For the symmetric slab modes (P4/mmm), the odd-parity member of the pair will be IR active, and the even-parity member will be Raman active.

Additionally, in a nanocrystal of below 10 nm, the translation symmetry is partially lost, and the selection rule of $q \approx 0$ is relaxed. In this situation, IR/Raman probes the active modes from the whole BZ in the nanocrystal, introducing additional broadening and possibly new peaks to the bulk spectrum. Such phenomena was described by the "phonon-confinement" model,[54] which describes phonons as wavepackets with spatial dimensions similar to the nanocrystal, with a Gaus-

sian localization function. Thus phonons with $q \neq 0$ now also contribute to the Raman spectrum. Because the phonon dispersion is not flat away from Γ point, shift and broadening in the Raman frequency are expected.

In the case of $CsPbI_3$, as the optical branches increase frequencies when going away from $\bar{\Gamma}$ point, we can expect a blue shift of the Raman peaks in nanocrystals compared to the bulk. Additional surface localized peaks are also likely to appear, including the ones identified as surface states in the phonon PDOS (1.2 THz $\bar{\Gamma}$-point mode), and Raman/IR active $\bar{M}$-point mode. (Table 1) Work has been done on identifying phase transition using temperature-dependent Raman spectra on perovskites quantum dots,[55,56] where the Raman shift was slightly different to the bulk. We believe future experimental studies of size-dependent Raman spectra in perovskites quantum dots will help validate the behaviour we predict in this work.

Conclusions

We have investigated the surface phonon dispersion of $CsPbI_3$ in cubic and yellow phase, respectively. We identify surface localized modes in the cubic phase that have distinct characteristics, and their corresponding Raman/IR activity. These modes include in-plane and out-of-plane displacements at $\bar{\Gamma}$-point, as well as octahedral tilting, Jahn-Teller distortion, and breathing modes at the Brillouin zone boundary. We discovered mode hardening of bulk Cs head-to-head instabilities due to the presence of the surface, which results in the polar in-plane distortions being the largest instability of the surface. These results show that surface has an important role in structural dynamics by modifying the phonon behaviors of the bulk, which provides a route to structure stabilization, as well as improved transport and optical properties at the surface. The presence of the surface also introduces additional Raman/IR peaks, which may serve as experimental signatures of the surface phonon modes.

Acknowledgments

L. Z. T. and R. X. Y was supported by the Molecular Foundry, a DOE Office of Science User Facility supported by the Office of Science of the U.S. Department of Energy under Contract No. DE-AC02-05CH11231. This research used resources of the National Energy Research Scientific Computing Center, a DOE Office of Science User Facility supported by the Office of Science of the U.S. Department of Energy under Contract No. DE-AC02-05CH11231.

References

(1) Kojima, A.; Teshima, K.; Shirai, Y.; Miyasaka, T. Organometal Halide Perovskites as Visible-Light Sensitizers for Photovoltaic. *J. Am. Chem. Soc.* **2009**, *131*, 6050–6051.

(2) Lee, M. M.; Teuscher, J.; Miyasaka, T.; Murakami, T. N.; Snaith, H. J. Efficient Hybrid Solar Cells Based on Meso-superstructured Organometal Halide Perovskites. *Science.* **2012**, *338*, 643–647.

(3) Yang, W. S.; Noh, J. H.; Jeon, N. J.; Kim, Y. C.; Ryu, S.; Seo, J.; Seok, S. I. High-performance photovoltaic perovskite layers fabricated through intramolecular exchange. *Science.* **2015**, *348*, 1234–1237.

(4) Nie, W.; Blancon, J.-C.; Neukirch, A. J.; Appavoo, K.; Tsai, H.; Chhowalla, M.; Alam, M. A.; Sfeir, M. Y.; Katan, C.; Even, J.; Tretiak, S.; Crochet, J. J.; Gupta, G.; Mohite, A. D. Light-activated photocurrent degradation and self-healing in perovskite solar cells. *Nature Communications* **2016**, *7*, 11574.

(5) Yuan, H.; Debroye, E.; Janssen, K. P.; Naiki, H.; Steuwe, C.; Lu, G.; Moris, M.; Orgiu, E.; Uji-i, H.; De Schryver, F.; Samori, P.; Hofkens, J.; Roeffaers, M. B. Degradation of Methylammonium Lead Iodide Perovskite Structures through Light and Electron Beam Driven Ion Migration. *J. Phys. Chem. Lett.* **2016**, *7*, 561–566.

(6) Li, Y.; Xu, X.; Wang, C.; Ecker, B.; Yang, J.; Huang, J.; Gao, Y. Light-Induced Degradation of CH3NH3PbI3 Hybrid Perovskite Thin Film. *The Journal of Physical Chemistry C* **2017**, *121*, 3904–3910.

(7) Wang, Q.; Chen, B.; Liu, Y.; Deng, Y.; Bai, Y.; Dong, Q.; Huang, J. Scaling behavior of moisture-induced grain degradation in polycrystalline hybrid perovskite thin films. *Energy Environ. Sci.* **2017**, *10*, 516–522.

(8) Bryant, D.; Aristidou, N.; Pont, S.; Sanchez-Molina, I.; Chotchunangatchaval, T.; Wheeler, S.; Durrant, J. R.; Haque, S. A. Light and oxygen induced degradation limits the operational stability of methylammonium lead triiodide perovskite solar cells. *Energy & Environ. Sci.* **2016**, *9*, 1655–1660.

(9) Ju, M.-G.; Chen, M.; Zhou, Y.; Dai, J.; Ma, L.; Padture, N. P.; Zeng, X. C. Toward Eco-friendly and Stable Perovskite Materials for Photovoltaics. *Joule* **2018**, *2*, 1231–1241.

(10) Nenon, D. P.; Christians, J. A.; Wheeler, L. M.; Blackburn, J. L.; Sanehira, E. M.; Dou, B.; Olsen, M. L.; Zhu, K.; Berry, J. J.; Luther, J. M. Structural and chemical evolution of methylammonium lead halide perovskites during thermal processing from solution. *Energy & Environ. Sci.* **2016**, *9*, 2072–2082.

(11) Protesescu, L.; Yakunin, S.; Bodnarchuk, M. I.; Krieg, F.; Caputo, R.; Hendon, C. H.; Yang, R. X.; Walsh, A.; Kovalenko, M. V. Nanocrystals of Cesium Lead Halide Perovskites ($CsPbX_3$, X = Cl, Br, and I): Novel Optoelectronic Materials Showing Bright Emission with Wide Color Gamut. *Nano Lett.* **2015**, *15*, 3692–3696.

(12) Swarnkar, A.; Marshall, A. R.; Sanehira, E. M.; Chernomordik, B. D.; Moore, D. T.; Christians, J. A.; Chakrabarti, T.; Luther, J. M. Quantum dot – induced phase stabilization of α $CsPbI_3$ perovskite for high-efficiency photovoltaics. *Science* **2016**, *354*, 92–95.

(13) Sutton, R. J.; Filip, M. R.; Haghighirad, A. A.; Sakai, N.; Wenger, B.; Giustino, F.;

Snaith, H. J. Cubic or Orthorhombic? Revealing the Crystal Structure of Metastable Black-Phase $CsPbI_3$ by Theory and Experiment. *ACS Energy Lett.* **2018**, *3*, 1787–1794.

(14) Wu, T.; Wang, Y.; Dai, Z.; Cui, D.; Wang, T.; Meng, X.; Bi, E.; Yang, X.; Han, L. Efficient and Stable CsPbI $_3$ Solar Cells via Regulating Lattice Distortion with Surface Organic Terminal Groups. *Advanced Materials* **2019**, 1900605.

(15) Marronnier, A.; Roma, G.; Boyer-Richard, S.; Pedesseau, L.; Jancu, J.-M.; Bonnassieux, Y.; Katan, C.; Stoumpos, C. C.; Kanatzidis, M. G.; Even, J. Anharmonicity and Disorder in the Black Phases of Cesium Lead Iodide Used for Stable Inorganic Perovskite Solar Cells. *ACS Nano* **2018**, *12*, 3477–3486.

(16) Haruyama, J.; Sodeyama, K.; Han, L.; Tateyama, Y. Termination Dependence of Tetragonal $CH_3NH_3PbI_3$ Surfaces for Perovskite Solar Cells. *J. Phys. Chem. Lett.* **2014**, *5*, 2903–2909.

(17) Zhou, H.; Chen, Q.; Li, G.; Luo, S.; Song, T.-b.; Duan, H.-S.; Hong, Z.; You, J.; Liu, Y.; Yang, Y. Interface engineering of highly efficient perovskite solar cells. *Science* **2014**, *345*, 542–546.

(18) Schulz, P.; Cahen, D.; Kahn, A. Halide Perovskites: Is It All about the Interfaces? *Chem. Rev.* **2019**, *119*, 3349–3417.

(19) Cao, D. H.; Stoumpos, C. C.; Farha, O. K.; Hupp, J. T.; Kanatzidis, M. G. Two-dimensional homologous perovskites as light absorbing materials for solar cell applications. *J. Am. Chem. Soc.* **2015**, *137*, 7843–7850.

(20) Stoumpos, C. C.; Cao, D. H.; Clark, D. J.; Young, J.; Rondinelli, J. M.; Jang, J. I.; Hupp, J. T.; Kanatzidis, M. G. Ruddlesden-Popper Hybrid Lead Iodide Perovskite 2D Homologous Semiconductors. *Chem. Mater.* **2016**, *28*, 2852–2867.

(21) Tsai, H. et al. High-efficiency two-dimensional ruddlesden-popper perovskite solar cells. *Nature* **2016**, *536*, 312–317.

(22) Dutta, A.; Dutta, S. K.; DasAdhikari, S.; Pradhan, N. Phase-Stable $CsPbI_3$ Nanocrystals: The Reaction Temperature Matters. *Angew. Chem. Int. Ed.* **2018**, *57*, 9083–9087.

(23) Kong, X.; Shayan, K.; Hua, S.; Strauf, S.; Lee, S. S. Complete Suppression of Detrimental Polymorph Transitions in All-Inorganic Perovskites via Nanoconfinement. *ACS Applied Energy Materials* **2019**, *2*, 2948–2955.

(24) Yang, R. X.; Skelton, J. M.; da Silva, E. L.; Frost, J. M.; Walsh, A. Assessment of dynamic structural instabilities across 24 cubic inorganic halide perovskites. *J. Chem. Phys.* **2020**, *152*, 024703.

(25) Yang, R. X.; Skelton, J. M.; da Silva, E. L.; Frost, J. M.; Walsh, A. Spontaneous Octahedral Tilting in the Cubic Inorganic Caesium Halide Perovskites CsSnX3 and CsPbX3 (X = F, Cl, Br, I). *J. Phys. Chem. Lett.* **2017**, *8*, 4720–4726.

(26) Yaffe, O.; Guo, Y.; Tan, L. Z.; Egger, D. A.; Hull, T.; Stoumpos, C. C.; Zheng, F.; Heinz, T. F.; Kronik, L.; Kanatzidis, M. G.; Owen, J. S.; Rappe, A. M.; Pimenta, M. A.; Brus, L. E. Local Polar Fluctuations in Lead Halide Perovskite Crystals. *Phys. Rev. Lett.* **2017**, *118*, 136001.

(27) Marronnier, A.; Lee, H.; Geffroy, B.; Even, J.; Bonnassieux, Y.; Roma, G. Structural Instabilities Related to Highly Anharmonic Phonons in Halide Perovskites. *J. Phys. Chem. Lett.* **2017**, *8*, 2659–2665.

(28) Beecher, A. N.; Semonin, O. E.; Skelton, J. M.; Frost, J. M.; Terban, M. W.; Zhai, H.; Alatas, A.; Owen, J. S.; Walsh, A.; Billinge, S. J. L. Direct Observation of Dynamic Symmetry Breaking above Room Temperature in Methylammonium Lead Iodide Perovskite. *ACS Energy Lett.* **2016**, *1*, 880–887.

(29) Bertolotti, F.; Protesescu, L.; Kovalenko, M. V.; Yakunin, S.; Cervellino, A.; Billinge, S. J. L.; Terban, M. W.; Pedersen, J. S.; Masciocchi, N.; Guagliardi, A. Coherent Nanotwins and Dynamic Disorder in Cesium Lead Halide Perovskite Nanocrystals. *ACS Nano* **2017**, *11*, 3819–3831.

(30) Stoumpos, C. C.; Malliakas, C. D.; Kanatzidis, M. G. Semiconducting Tin and Lead Iodide Perovskites with Organic Cations: Phase Transitions, High Mobilities, and Near-Infrared Photoluminescent Properties. *Inorg. Chem.* **2013**, *52*, 9019–9038.

(31) Hong, J.; Prendergast, D.; Tan, L. Z. Layer Edge States Stabilized by Internal Electric Fields in Two-Dimensional Hybrid Perovskites. *Nano Letters* **2021**, *21*, 182–188, PMID: 33125252.

(32) Lao, X.; Zhou, W.; Bao, Y.; Wang, X.; Yang, Z.; Wang, M.; Xu, S. Photoluminescence signatures of thermal expansion, electron–phonon coupling and phase transitions in cesium lead bromide perovskite nanosheets. *Nanoscale* **2020**, *12*, 7315–7320.

(33) Khoo, K. H.; Zayak, A. T.; Kwak, H.; Chelikowsky, J. R. First-Principles Study of Confinement Effects on the Raman Spectra of Si Nanocrystals. *Phys. Rev. Lett.* **2010**, *105*, 115504.

(34) Louren ço Martins, H.; Kociak, M. Vibrational Surface Electron-Energy-Loss Spectroscopy Probes Confined Surface-Phonon Modes. *Phys. Rev. X* **2017**, *7*, 041059.

(35) Hwang, Y.-N.; Park, S.-H.; Kim, D. Size-dependent surface phonon mode of CdSe quantum dots. *Physical Review B* **1999**, *59*, 7285–7288.

(36) Kresse, G.; Furthmüller, J. Efficiency of Ab-initio Total Energy Calculations for Metals and Semiconductors Using a Plane-wave Basis Set. *Comput. Mater. Sci.* **1996**, *6*, 15–50.

(37) Kresse, G.; Furthmüller, J. Efficient Iterative Schemes for Ab Initio Total-energy Calculations Using a Plane-wave Basis Set. *Phys. Rev. B* **1996**, *54*, 11169–11186.

(38) Perdew, J. P.; Ruzsinszky, A.; Csonka, G. I.; Vydrov, O. A.; Scuseria, G. E.; Constantin, L. A.; Zhou, X.; Burke, K. Restoring the Density-Gradient Expansion for Exchange in Solids and Surfaces. *Phys. Rev. Lett.* **2008**, *100*, 136406.

(39) Perdew, J. P.; Ruzsinszky, A.; Csonka, G. I.; Vydrov, O. A.; Scuseria, G. E.; Constantin, L. A.; Zhou, X.; Burke, K. Erratum: Restoring the Density-gradient Expansion for Exchange in

Solids and Surfaces (Physical Review Letters (2008) 100 (136406)). *Phys. Rev. Lett.* **2009**, *102*, 39902.

(40) Bergerhoff, G.; Hundt, R.; Sievers, R.; Brown, I. D. The Inorganic Crystal Structure Data Base. *J. Chem. Inf. Comput. Sci.* **1983**, *23*, 66–69.

(41) Yang, R. X.; Tan, L. Z. Understanding size dependence of phase stability and band gap in $CsPbI_3$ perovskite nanocrystals. *J. Chem. Phys.* **2020**, *152*, 034702.

(42) Togo, A.; Tanaka, I. First Principles Phonon Calculations in Materials Science. *Scr. Mater.* **2015**, *108*, 1–5.

(43) Allen, P. B.; Berlijn, T.; Casavant, D. A.; Soler, J. M. Recovering hidden Bloch character: Unfolding electrons, phonons, and slabs. *Phys. Rev. B* **2013**, *87*, 085322.

(44) Aroyo, M. I.; Kirov, A.; Capillas, C.; Perez-Mato, J. M.; Wondratschek, H. Bilbao Crystallographic Server. II. Representations of crystallographic point groups and space groups. *Acta Crystallogr. A* **2006**, *62*, 115–128.

(45) Grisorio, R.; Clemente, M. E. D.; Fanizza, E.; Allegretta, I.; Altamura, D.; Striccoli, M.; Terzano, R.; Giannini, C.; Irimia-Vladu, M.; Suranna, G. P. Exploring the surface chemistry of cesium lead halide perovskite nanocrystals. *Nanoscale* **2019**, *11*, 986–999.

(46) Liu, M. et al. Lattice anchoring stabilizes solution-processed semiconductors. *Nature* **2019**, *570*, 96–101.

(47) Roma, G. Modeling the contribution of point defects to the Raman spectrum of crystalline materials. *Model. Simul. Mater. Sci. Eng.* **2019**, *27*, 074001.

(48) Kurt, A. Pressure dependence of the Raman modes for orthorhombic and monoclinic phases of CsPbI3 at room temperature. *J. Appl. Phys* **2020**, *128*, 075106.

(49) Yang, Y.; Robbins, J. P.; Ezeonu, L.; Ma, Y.; Sparta, N.; Kong, X.; Strauf, S.; Podkolzin, S. G.; Lee, S. S. Probing lattice vibrations of stabilized CsPbI3 polymorphs via low-frequency Raman spectroscopy. *J. Mater. Chem. C* **2020**, *8*, 8896–8903.

(50) Satta, J.; Melis, C.; Carbonaro, C. M.; Pinna, A.; Salado, M.; Salazar, D.; Ricci, P. C. Raman spectra and vibrational analysis of CsPbI3: A fast and reliable technique to identify lead halide perovskite polymorphs. *J. Materiomics* **2021**, *7*, 127–135.

(51) Forbes, B. D.; Allen, L. J. Modeling energy-loss spectra due to phonon excitation. *Phys. Rev. B* **2016**, *94*.

(52) Lagos, M. J.; Trügler, A.; Hohenester, U.; Batson, P. E. Mapping vibrational surface and bulk modes in a single nanocube. *Nature* **2017**, *543*, 529–532.

(53) Dresselhaus, M. S.; Dresselhaus, G.; Jorio, A. *Group Theory: Application to the Physics of Condensed Matter*; Springer-Verlag: Berlin Heidelberg, 2008.

(54) Richter, H.; Wang, Z.; Ley, L. The one phonon Raman spectrum in microcrystalline silicon. *Solid State Commun.* **1981**, *39*, 625–629.

(55) Zhou, W.; Sui, F.; Zhong, G.; Cheng, G.; Pan, M.; Yang, C.; Ruan, S. Lattice Dynamics and Thermal Stability of Cubic-Phase CsPbI $_3$ Quantum Dots. *The Journal of Physical Chemistry Letters* **2018**, *9*, 4915–4920.

(56) Liao, M.; Shan, B.; Li, M. In Situ Raman Spectroscopic Studies of Thermal Stability of All-Inorganic Cesium Lead Halide ($CsPbX_3$, X = Cl, Br, I) Perovskite Nanocrystals. *J. of Phys. Chem. Lett.* **2019**, *10*, 1217–1225.